Muon g-2 storage ring beam and spin dynamics

Editors: J. D. Crnkovic,[1,*] D. W. Hertzog,[2] W. M. Morse,[1] and D. Stratakis[3]
(Muon $g-2$ Collaboration)

[1] *Brookhaven National Laboratory, Upton, New York 11973-5000, USA*
[2] *Department of Physics, University of Washington, Seattle, Washington 98195-1560, USA*
[3] *Fermi National Accelerator Laboratory, Batavia Illinois 60510-5011, USA*

(Dated: June 24, 2019)

Jason

The goal of the new $g-2$ experiment at Fermilab is a measurement of the anomalous magnetic moment of the muon, with uncertainty of less than 140 parts-per-billion. The experimental method is to store a beam of polarized muons in a storage ring with pure vertical dipole field and electrostatic focusing, and to measure the precession frequency. Control of the systematics depends on unprecedented knowledge of the details of the phase space of the muon distribution. That knowledge is derived from direct measurements with scintillating fiber detectors that are inserted into the muon beam for diagnostic measurements, traceback straw tube tracking chambers, as well as the calorimeters that measure energy, time and position of the decay positrons. The interpretation of the measurements depends on a detailed model of the storage ring guide field. This invited talk presents results of studies of the distribution from the commissioning run of the experiment.

I. INTRODUCTION

Jason

The muon magnetic moment is a property that can be calculated in the context of the standard model of particle physics. A comparison of the measured and predicted anomaly is a grand test of the model. The goal of the experiment is to measure the anomaly with 140 part-per-billion (ppb) precision.

The experimental method is to circulate a beam of polarized muons in a storage ring and to measure the precession frequency, or rather the difference between the precession frequency and the revolution frequency, ω_a, the spin tune. The $3.094\,\mathrm{GeV}/c$ momentum muons decay with lifetime of about $64\,\mu\mathrm{s}$ in the lab frame to a positron and a pair of neutrinos. The energy of the positron in the lab frame is correlated with the polarization of the parent muon. The variation in the number of high energy positrons with time is the measure of ω_a.

The frequency with which the muons precess depends on the details of the magnetic and electric guide field of the storage ring. Magnetic focusing is evidently precluded as it would introduce an unacceptable variation in the magnetic field across the storage volume. Instead vertical focusing is provided by electrostatic quadrupoles. The muon momentum is chosen to minimize the effect of the electric field on the precession frequency. Indeed, at the muon magic momentum, $3.094\,\mathrm{GeV}/c$, the contribution of the electric field to the difference frequency vanishes.

We describe the electric and magnetic guide field of the 44.69 m circumference storage ring, the lattice functions and the process for injecting and storing polarized muons. The detector systems that inform the beam distributions are introduced. The contributions to ω_a that arise from finite beam width and length, momentum spread, and coherent oscillation of the centroid are described, as are the measurements of the distributions that are essential to accounting for the effects.

II. EXPERIMENTAL METHOD

A. Polarized Muon Production

Diktys

The π^+ decay to $\mu^+ + \bar{\nu}_\mu$. The pion has zero spin and the neutrino is always right handed. In the pion rest frame the μ^+ is also right handed. To conserved angular momentum. Boost to lab frame. The muons with momentum in the same direction as the pi in the lab frame will be all right handed. Muons with momentum antiparallel to the pi will end up left handed. And lower momentum. By selecting the highest momentum muons we get a polarized beam, order 95 %.

B. Spin Precession

Jason

Elaborate on the spin precession.

Muons decay to $\mu^+ \to e^+ + \bar{\nu}_\mu + \nu_e$. The muon spin is correlated with the momentum of the electron in the lab frame. In the muon rest frame the spin is in the z direction. The total final state momentum is the sum of neutrinos and positron. The max momentum of the final state positron is when neutrinos have the same momentum (same direction) and the positron has equal but

* jcrnkovic@bnl.gov

opposite. Since the spin of the neutrinos is equal but opposite, the positron carries off the angular momentum of the muon. The e^+, an anti-lepton is most likely to be right handed in a weak decay, and therefore with momentum in the same direction as that of the muon spin. The positron with minimum momentum in the muon rest frame will be when neutrinos are in opposite directions, with total spin 1 and the positron has near zero momentum and the spin opposite that of the muon. It is as before most likely to be right handed, and therefore to have momentum opposite to the muon spin. The result is that in the lab frame, positron momenta is correlated with muon spin. The measurement is by counting the time dependence of the number of high momentum decay positrons. The experiment is equipped with calorimeters that measure the number vs time of high momentum positrons. The muon has equal but opposite momentum to the neutrinos and necessarily the muon spin. The detector acceptance depends on the transverse position of the decay muon. Therefore acceptance varies with the betatron and dispersive variation of the distribution in phase space of the muon beam.

Momentum of the positron is correlated with the muon spin. Measurement of decay positron momentum as function of time is precession frequency. Focusing is the dipole field and electrostatic quads. So as not to introduce a field variation. But the E-field couples to the magnetic moment anyway. If the dimensionless g-factor of the muon were identically 2, then in any magnetic field the spin will stay synched with the trajectory independent of its momentum. In an electric field, if $g = 2$, then at $\beta \ll 1$ there is no effect on the polarization and polarization is fixed independent of trajectory. At $\gamma \gg 1$ the magnetic field in the rest frame of the muon is $B \to cE$ and the spin is again pinned to the trajectory. Since $g > 2$ the spin rotates more rapidly than the trajectory. There is a momentum, the so-called magic momentum, where the spin follows the trajectory. And for the muon that is at $\gamma = 29.3$. The spin is frozen to the direction in an electric field. By operating at the magic momentum, the E-field the precession is decoupled from the E-field.

The expression for the anomalous precession frequency, in the limit of vanishing longitudinal magnetic field, is

$$\vec{\omega}_a = -\frac{q}{m}\left[a_\mu \vec{B} - a_\mu \left(\frac{\gamma}{\gamma+1}\right)\left(\vec{\beta}\cdot\vec{B}\right) - \left(a_\mu - \frac{1}{\gamma^2-1}\right)\frac{\vec{\beta}\times\vec{E}}{c}\right]. \tag{1}$$

For muons at magic momentum ($p_0 = m/\sqrt{a_\mu}$) circulating on the design orbit,

$$\vec{\omega}_a = -\frac{q}{m} a_\mu \vec{B}.$$

TABLE I: Jason Muon $g-2$ storage ring magnet parameters.

Parameter	Value
Nominal Magnetic Field	1.4513 T
Nominal Current	5200 A
Equilibrium Orbit (Magic) Radius	7112 mm
Muon Storage Region Radius	45 mm
Magnet Gap Length	180 mm
Nominal Stored Energy	6 MJ

C. Precision Magnetic Field

Jason

Elaborate on the high precision magnetic field, see Table I and Fig. 1.

III. STORAGE RING

Renee

The $g-2$ storage ring is a weak focusing machine with a single adjustable parameter, namely the quadrupole voltage, that determines horizontal and vertical tunes, as well as the β and dispersion (η) functions. Figure 2 shows the layout of the ring. The quads [**?**] are vertically focusing and horizontally defocusing. In the limit where $V_{\rm quad} \to 0$, the horizontal tune is unity and vertical is zero. With increasing voltage the vertical tune increases and horizontal decreases.

Three distinct detector systems inform the muon distribution. Twenty-four calorimeters [**?**], distributed uniformly around the inner circumference of the ring, measure energy, position and time of decay positrons. There are two tracking stations [**?**], located 180° and 270° from the injection point, comprised of straw wire chambers, that measure the trajectory of the decay positron. The reconstructed track is then traced back to reveal the position of the parent muon. The fiber harp system provides the most direct measure of the circulating muons. Each of the four harps consists of seven 0.5 mm diameter parallel scintillating fibers with 13 mm spacing. There are two horizontal and two vertically oriented harps at 180° and 270° respectively. The fiber harps [**?**] are rotated into the beam to measure time dependence of beam centroid and profile, and are retracted during production running.

The fiber harps and the tracking detectors provide complimentary measurements of motion of the centroid (Figs. 3 and 4) and modulation of the width, Fig. 5.

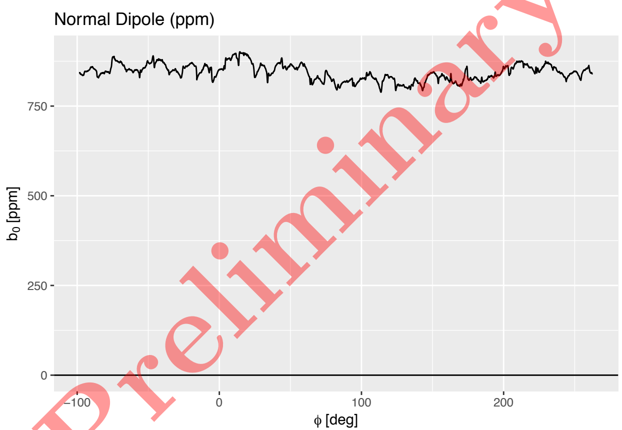

(a) Dipole magnetic field.

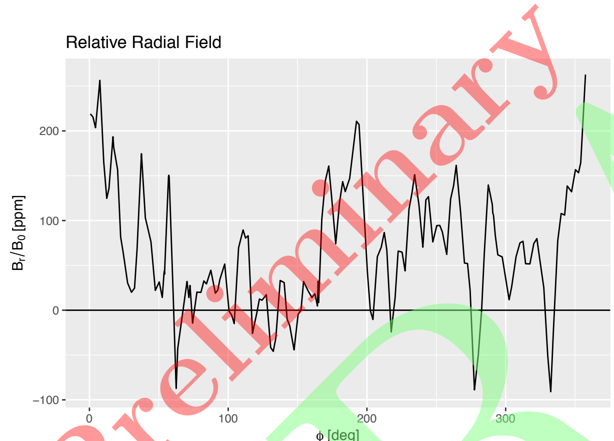

Surface coils have been tweaked to reduce the $\langle y \rangle$ around the ring. To simulate, we take the radial data from 2016 *minus* 35 ppm, according to most recent shimming.

(b) Radial magnetic field.

FIG. 1: Mike Preliminary storage ring magnetic field data. *Maybe we should show preliminary field data, as it is used to calculate closed orbit distortions.*

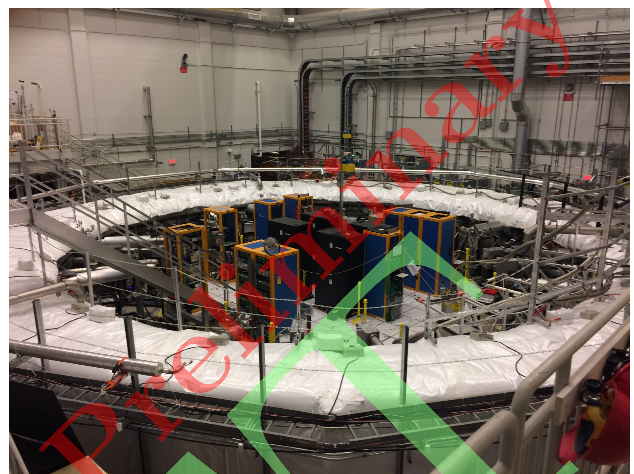

(a) Annotated storage ring picture *[still need to annotate the picture]*.

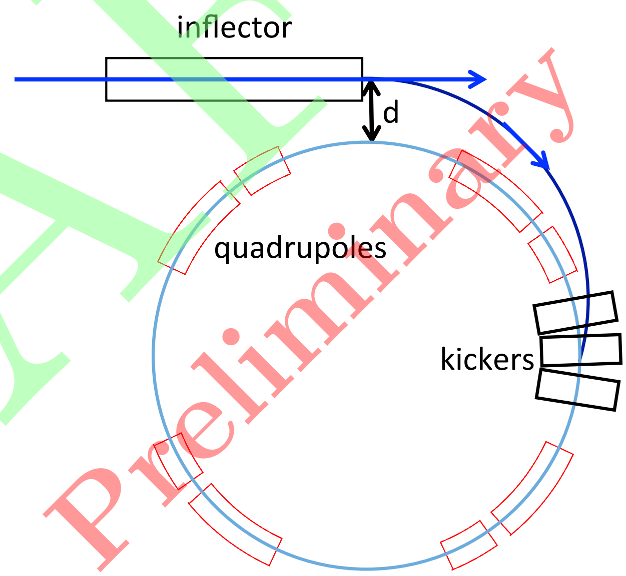

(b) Storage ring diagram.

FIG. 2: Jason Injected beam enters the $g-2$ ring through a hole in the back leg iron. It emerges from the back leg and enters the inflector which cancels the field of the storage ring magnet. Beam exits the inflector, and enters the ring through the kicker gap. The circumference of the ring is 44.69 m (revolution period 149 ns). The 1.45 T bending field is continuous around the ring.

IV. SIMULATION TOOLS

A. G4beamline

Diktys

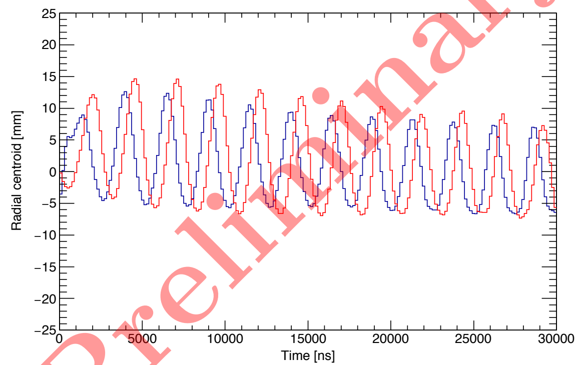

FIG. 3: David R. Horizontal position of centroid measured with the 180° fiber harp (blue) and 270° harp (red) for the first 30 µs of the fill. A discrete Fourier transform yields the horizontal tune.

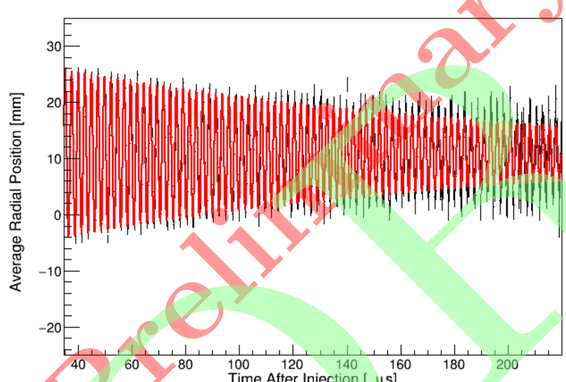

FIG. 4: David R. Radial centroid as measured with the 180° tracker over the first 220 µs of the fill. Red curve is a fitted damped sinusoid. Measurement is increasingly noisy at longer times as statistics are limited.

B. Phase Space Models

Mike

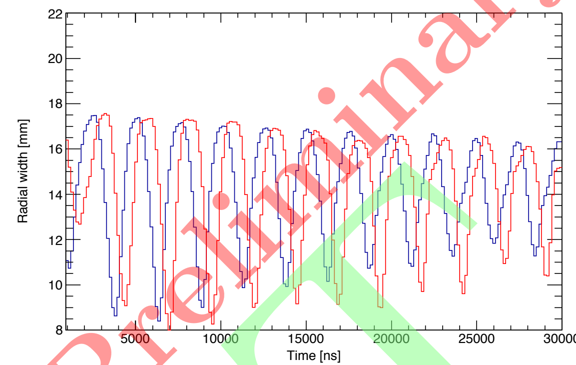

FIG. 5: David R. Horizontal width at 180° harp (blue) and 270° harp (red) over the first 30 µs of the fill. The deep modulation is a combination of β and η mismatch.

C. gm2ringsim

Renee

D. Bmad

David R. BMAD refers to a subroutine library[?] for simulating the dynamics of relativistic beams of charged particles, and an associated format for defining beam line components. As long as the guide field components are defined according to BMAD conventions, the full complement of the analysis tools of the library can be used to investigate the particle dynamics, including various tracking methods, (Taylor maps, symplectic integration, Runge Kutta), construction of maps from tracking, evaluation of Twiss parameters, tracking through maps defined by maps or multipoles, etc. (For details see Bmad-Manual).

The BMAD formatted representation of the g-2 experiment is comprised of three distinct branches, 1)M5 beam line, 2)the injection channel through the backleg iron and inflector, and the 3)storage ring including DC magnetic field, time dependent quadrupole electric fields and kicker magnetic fields, and collimator apertures. In the language of BMAD, 'branches' are joined at 'fork' elements and offsets with 'patches'.

The beam lines are assembled as a sequence of elements with fixed length. The electro-magnetic fields in each element are defined by field maps, multipole expansions, or analytic expressions. Time dependence for pulsed kickers and ramped quadrupoles requires custom code (as there is no appropriate standard BMAD module). Specialized custom routines can apply arbitrary kicker pulse shapes or quadrupole voltage time dependence.

Particle phase space and spin are tracked through the guide field using runge-kutta integration.

The program is equipped with a module to generate an initial distribution of muons, or to read a distribution from a file or both. For example, it is possible to generate a distribution gaussian in transverse phase space, with longitudinal distribution read from a file. (This is useful for imprinting the 'W' shaped longitudinal distribution on an otherwise gaussian transverse distribution.)

Lattice and phase space parameters are computed with standard BMAD routines, including twiss parameters, beam moments, closed orbits, betatron tunes, chromaticity, synchrotron radiation, spin tunes, etc. The Jacobian matrices required to determine tunes and twiss parameters are based on tracking.

Scattering is somehwat ad hoc. Muons entering the storage volume on trajectories that pass through quad plates, multple scatter in the plates. Muons that are already inside the storage volume are lost if their trajectory subsequently intercepts a quad plate or collimator. If fiber monitors are active, muons multiply scatter in the fibers with energy loss consistent with measurements.

If the muon decay is turned on, then muons decay with lifetime assigned at birth. The phase space, spin coordinates and time of the decay at the decay point are recorded. A positron is created with momentum four-vector appropriately correlated with muon spin. The positron is tracked until it strikes a calorimeter plane, where phase space coordinates and time are recorded, or otherwise leaves the storage volume.

The walls of the inflector are defined as continuous apertures. Particles that hit the walls are lost. The ends of the inflector are treated as scattering planes.

E. Quadrupoles

The quadrupole plates are curved to preserve a fixed radial offset with respect to the central on momentum design orbit. The curvilinear coordinate system can be represented by beginning with a full 3-dimensional map, and then extracting an azimuthal slice of the map (in r, z at fixed ϕ) or with a fitted multipole expansion of McMillan functions. The curvature necessarily introduces nonlinearities that are not faithfully included in a 2 dimensional cartesian expansion. The BMAD code allows several possible ways to specify the quadrupole electric field.

1. Field map. The field map that is currently incorporated is based on a ρ, z azimuthal slice of of a 3 dimensional OPERA map. The quad map can be optionally defined as the sum of individual maps for each of the four plates, thus providing the flexibility to set the voltage independently on each plate, to model voltage errors, or the scraping configuration.
2. Multipole expansion. The multipole expansion in McMillan functions is derived as a fit to the azimuthal slice of the 3 dimensional map. An expansion in cartesian coordinates (that is inconsistent with Maxwell in the curved geometry) is another option. The multipole representations are convenient for exploring dependence on nonlinearity.

F. Main magnet

The main magnet is represented as a map or analytic function with uniform field. A unform radial component can be specified. Measured field errors are incorporated analytically. The azimuthal dependence of the error field is expanded as a solution to Laplace's equation in cylindrical coordinates in order to ensure consistency with Maxwell equations.

G. Injection channel

The magnetic field through the hole in the back leg iron and cryostat and main magnet fringe field is based on a 3 dimensional OPERA map. A distinct map is computed for the field in the inflector. The fringe and inflector maps are superimposed as appropriate.

The BMAD model has been used extensively to explore dependencies (capture efficiency, CBO amplitude, phase space distribution of captured beam, etc.) on injection trajectory, inflector orientation, field and aperture, kicker field amplitude, field profile, pulse shape, and timing, and quad voltage. Effects of quad field errors and misalignment on closed orbit and twiss parameters have been studied. Simulations informed analysis of measurements with fiber harps. The flexibility to employ various quadrupole field profiles has enabled study of effects of nonlinearities on decoherence and debunching, electric field and pitch corrections. Indeed simulation will play a critical role in evaluation of the electric field and pitch systematics.

H. COSY INFINITY

Martin

V. STORAGE RING OPTICS

Martin

Figure 6 shows horizontal and vertical unes along the voltage contour. The β and η functions for quad voltage of 20.4 kV are shown in Fig. 7. *Someone should say something about the dependence of Twiss parameters on V_{quad}, see Fig. 8.*

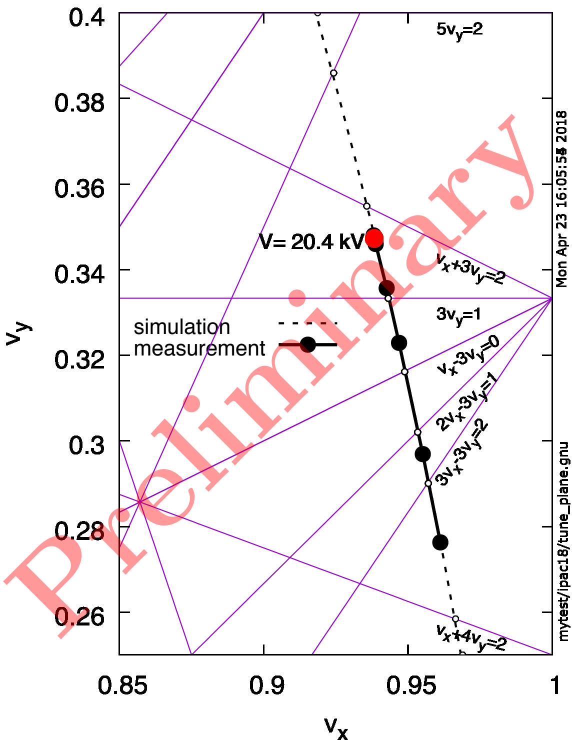

FIG. 6: Jason Dependence of tune on quadrupole voltage computed with a Bmad[?] based model of the guide field. Resonance lines are shown. Tentative operating point is 20.4 kV (red dot).

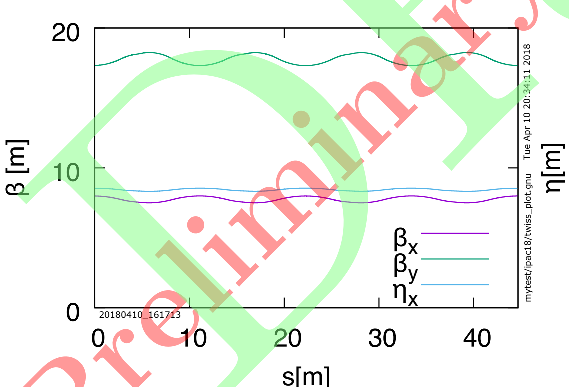

FIG. 7: David R. and David T. Twiss parameters in the closed storage ring *[See DocDB16661]*.

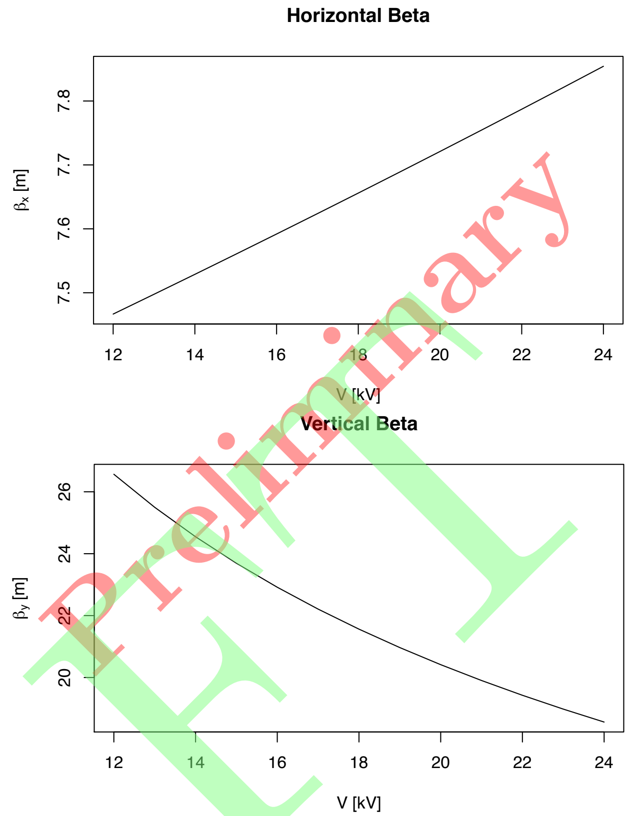

(a) Beta function dependence on quadrupole voltage.

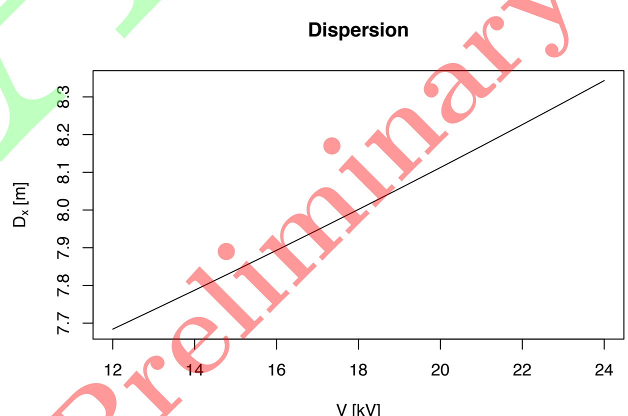

(b) Dispersion function dependence on quadrupole voltage.

FIG. 8: Mike and David T. Twiss parameter dependence on quadrupole voltage (V_{quad}). *See DocDB15538 and DocDB16661; Need to combine into a single figure. Needs to specify if this is the max or something else.*

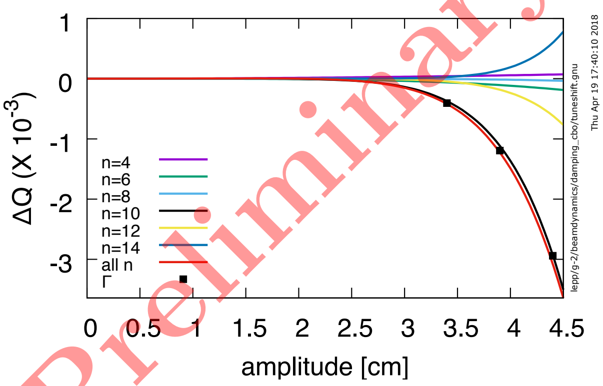

FIG. 9: David R. Simulated contribution to amplitude dependent tune shift from each of the quad multipoles, their sum, and the decoherence rate Γ as determined by tracking.

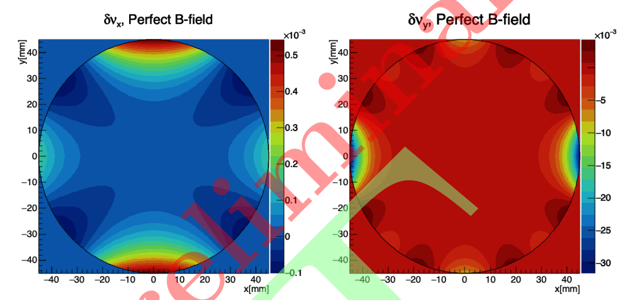

(a)

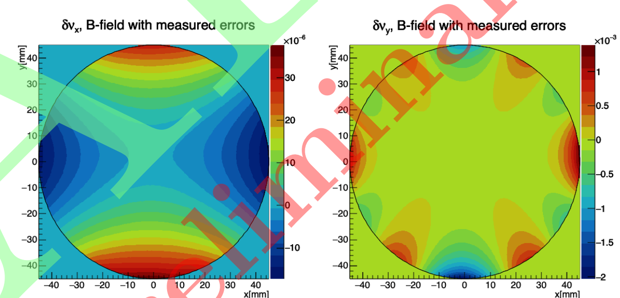

(b)

FIG. 10: David T. Amplitude-dependent tune shifts ($\delta p/p_0 = 0$, $p_x/p_0 = 0$, $p_y/p_0 = 0$) within the storage region ($r \leq 45$ mm) for an ideal (a) and measured (b) magnetic field.

The quadrupole field is superimposed on the main dipole field. The reference trajectory through the quadrupoles has significant curvature and the quadrupoles share that curvature. As a result, the quadrupole field is necessarily nonlinear, with a significant sextupole term. An effect of this and other nonlinearities associated with the geometry of the quad electrodes is an amplitude dependence of the tunes. The tune shifts associated with the various quad multipoles [**?**] are shown in Fig. 9. Figure 10 shows that the magnetic field imperfections also lead to amplitude-dependent tune shifts. The magnetic field *Someone should say something about the tune dependence on momentum and chromaticity dependence on quadrupole voltage, see Figs. 11 and 12.* The nonlinearities of the electrostatic quadrupoles, as well as residual magnetic multipoles [**?**] can drive resonances (see Fig. 6). Operation near resonances is avoided to mitigate losses. A tune scan that extends over the operating region is shown in Fig. 13. The storage fraction is measured as quadrupole voltage is increased from 18 kV to 23 kV. The degraded storage fractions evident at 18.8 kV and 21.2 kV correspond to the $3\nu_x = 1$ and $\nu_x + 3\nu_y = 2$ resonances.

The guide field is characterized by measurements of closed orbit, tunes, and modulation of the beam width and centroid. Measurements of the tunes with the fiber harps are shown in Fig. 6. *Someone should say something about the tune footprint, see Fig. 14.*

A. Injection

Diktys (beamline) David R. (through the inflector)

The beam is injected into the ring through a hole in the back leg iron. The 1.7 m long superconducting inflector bucks the main dipole field so that the beam traverses the inflector without significant deflection and exits the inflector on a trajectory tangent to a displaced circular orbit. The beam crosses the design orbit in the gap of

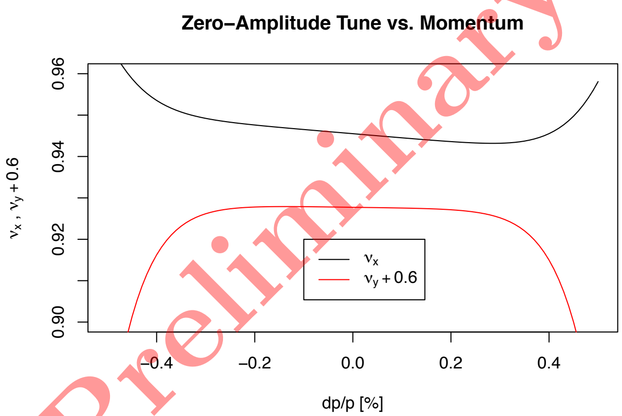

(a) Tune value vs. relative momentum.

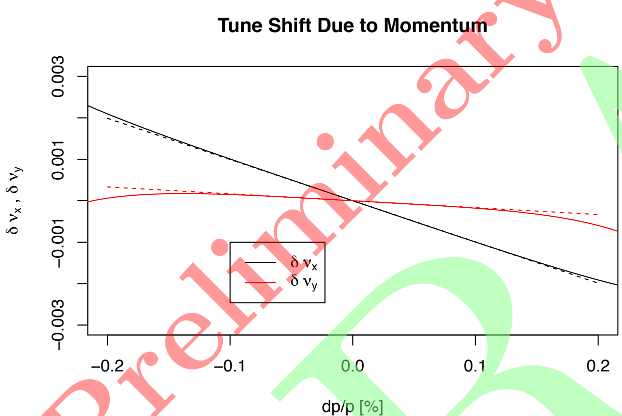

(b) Tune shift vs. relative momentum.

FIG. 11: Mike and David T. Tune dependence on muon momentum *[See DocDB15538 and DocDB16661]*.

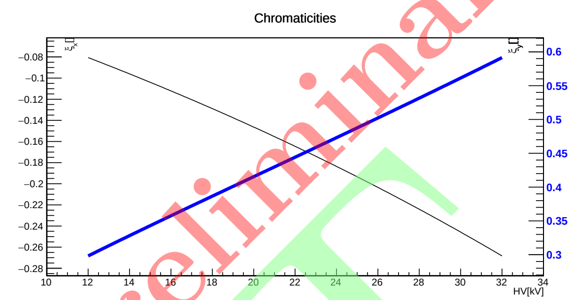

FIG. 12: David T. Chromaticity dependence on quadrupole voltage.

the pulsed kicker that steers the beam radially outward and onto the central orbit as shown in Fig. 2.

The inflector aperture (18 mm horizontally by 56 mm vertically) is very much smaller than the aperture of the ring (90 mm round). In order to maximize transmission, the beam is focused to a narrow waist through the inflector and with zero dispersion.

Manipulation of the beam width to maximize transmission through the inflector and into the ring is illustrated in Fig. 15. The mismatch of β and η functions leads to a modulation of beam width with components at the betatron frequency and twice the betatron frequency respectively. The relative contribution of betatron motion and momentum offset to the width can be extracted from the width measurement (Fig. 5) by suitable decomposition. The phase space at the inflector exit is defined by the inflector aperture and shown in Figs. 16.

The kicker is located $\phi_\beta = \pi/2$ downstream from the injection point at the inflector exit. The beam crosses the design orbit with an angle determined by the radial displacement of the inflector axis (nominally 77 mm from the design orbit and indicated as 'd' in Fig. 2), and the exit angle. The crossing angle, and therefore the kick required to steer the beam onto the closed orbit, is minimum if the exit angle is zero. The dependencies can be made quantitative with a few simplifying assumptions, namely that the β and η functions are uniform around the ring, and as long as we treat the kickers as a δ-function in azimuthal angle. (The kickers [? ?] in fact extend over about 36° of arc). With these assumptions, the horizontal displacement of the trajectory is

$$\begin{aligned} x(s) &= (x_{\text{inf}} - \delta\eta)\cos[\phi(s)] + \eta\delta \\ &\quad - k\beta_0 \cos[\phi(s)] + x'_{\text{inf}} \sin[\phi(s)] \\ &= A\cos[\phi(s) + \phi_0] + \eta\delta, \end{aligned}$$

where $x_{\text{inf}}, x'_{\text{inf}}$ are the displacement and angle of the trajectory at the inflector exit, η the dispersion, δ is the fractional momentum offset, k is the kick angle, $\phi(s)$ the betatron phase advance with $s = 0$ at the injection point,

$$A = \pm\sqrt{(x_{\text{inf}} + \delta\eta - k\beta)^2 + (x'_{\text{inf}}\beta)^2}$$

$$\tan\phi_0 = \frac{x'_{\text{inf}}\beta}{x_{\text{inf}} - \delta\eta - k\beta}.$$

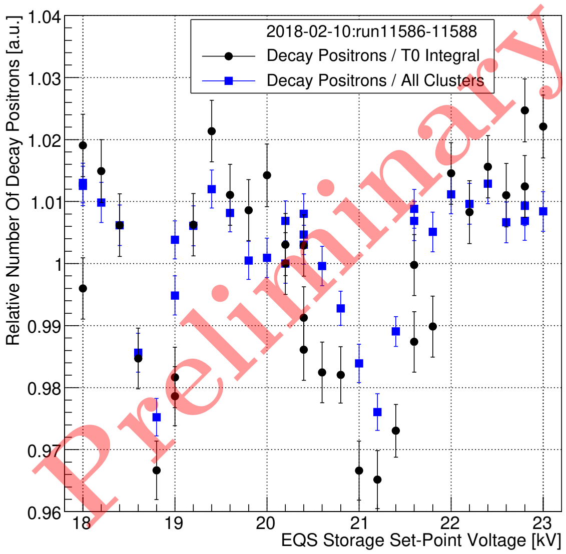

(a)

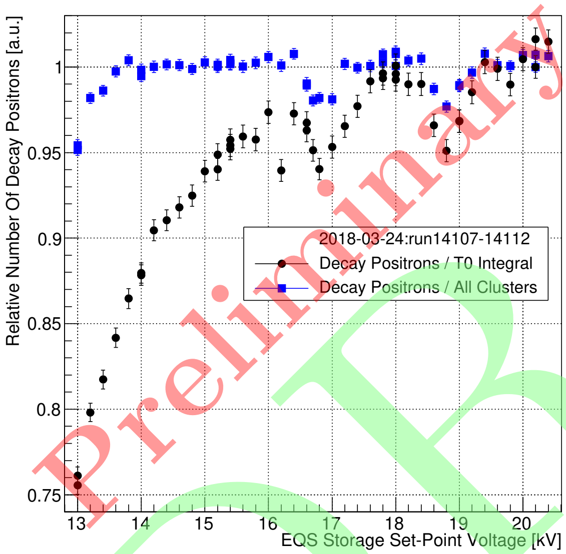

(b)

FIG. 13: Jason Relative number of decay positrons in a fill as a function of quadrupole voltage *[remove run numbers and renormalize to 20.4 kV setting]*. Storage efficiency is degraded by betatron resonances at 18.8 and 21.2 kV.

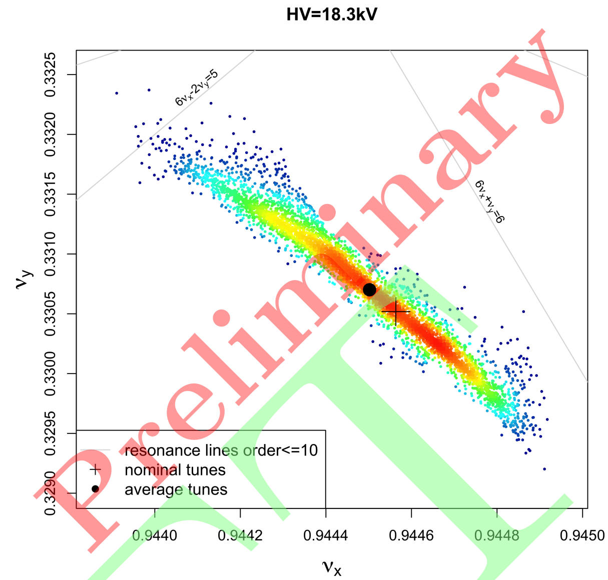

FIG. 14: David T. Tune footprint of a beam distribution at 149 μs after injection and for a magnetic field measurement.

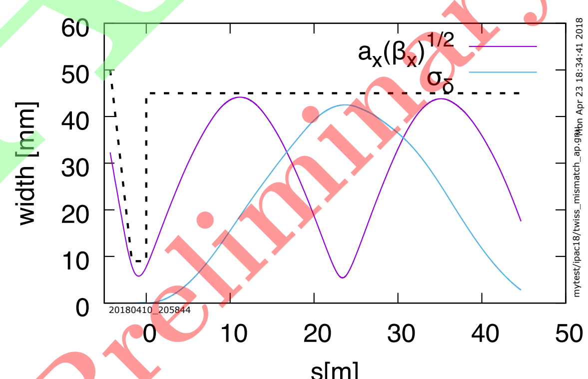

FIG. 15: David R. Propagating beam betatron and energy width through narrow aperture inflector and into the storage ring. The dashed line is the horizontal aperture.

The extremes of the displacement of the motion, that is the envelope of the motion is given by $x_{\text{ext}} = \pm|A| + \eta\delta$. The envelope is plotted in Fig. 17 as a function of momentum for three different injection angles, and for a kick angle $k = 8$ mrad, which is about 80 % of the nominal kick, and Fig. 18 for the nominal kick of $k = 10.8$ mrad.

The minimum momentum that can be stored decreases as the kicker angle approaches nominal. Under kicking skews the momentum distribution high. Kick and and injection angle both contribute to the amplitude of the oscillations about the closed orbit. Non zero injection angle reduces momentum acceptance symmetrically about

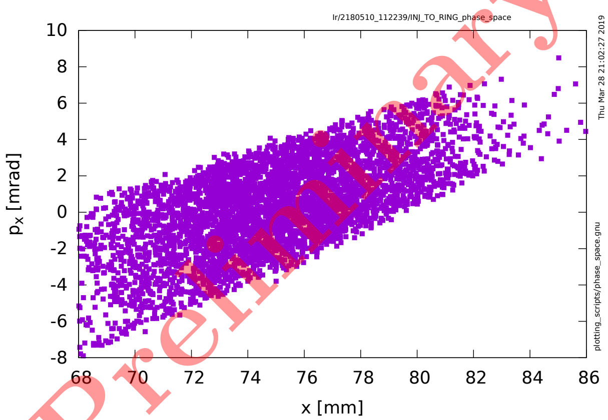

(a) Horizontal phase space at the exit of the inflector.

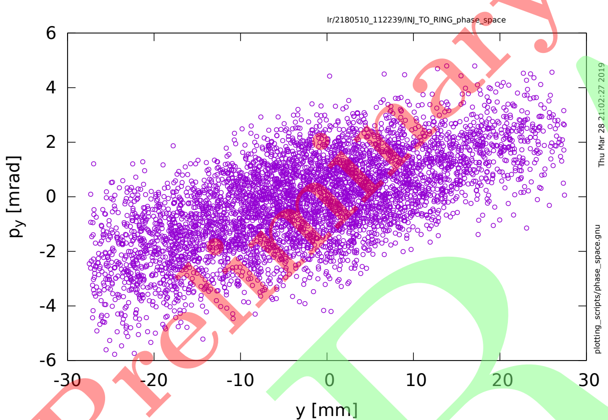

(b) Vertical phase space at the inflector exit.

FIG. 16: David R. Simulated muon beam phase space at the downstream end of the inflector [be careful with the coordinate systems].

zero.

B. Tune Measurements

Jason

The horizontal (ν_x) and vertical (ν_y) tunes are defined

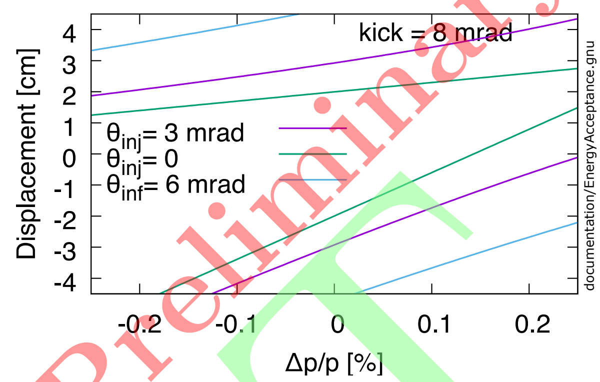

FIG. 17: David R. Kick angle ~80 % of nominal. The green lines mark the envelope of the motion of a muon that exits the inflector with zero angle. The on momentum muon oscillates between ±2 cm. If momentum offset is 0.2 % the peak to peak oscillation is ~5 mm. A muon with momentum offset of −0.18 % is outside the 4.5 cm aperture.

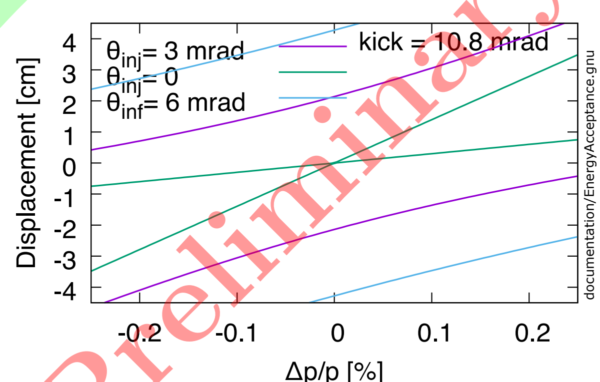

FIG. 18: David R. For the nominal kick angle (10.8 mrad), the trajectory of the on momentum muon coincides with the closed orbit. The on momentum muon injected with angle of ±3 mrad will oscillate within a ±2 cm envelope.

TABLE II: Jason Measured $\langle f_c \rangle$ and $\langle f_{\text{cbo}} \rangle$ (only statistical errors are given) and corresponding $\langle \nu_x \rangle$ calculated via Eq. (2). This data was collected during Run-1. The FBM measurements use the 6 o'clock horizontal FBM central fiber (no. 4), where the first 3 µs of data are not used for these measurements.

Detector	V_{quad} [kV]	$\langle f_c \rangle$ [MHz]	$\langle f_{\text{cbo}} \rangle$ [MHz]	$\langle \nu_x \rangle$
FBM	13.0	6.697(5)	0.2600(30)	0.9612(4)
FBM	15.0	6.697(5)	0.3005(30)	0.9551(4)
trackers	15.0	???	???	???
calorimeters	15.0	???	???	???
FBM	17.6	6.697(5)	0.3553(30)	0.9469(4)
trackers	18.3	???	???	???
calorimeters	18.3	???	???	???
FBM	19.0	6.697(5)	0.3845(30)	0.9426(5)
FBM	20.2	6.697(5)	0.4100(30)	0.9388(5)
trackers	20.4	???	???	???
calorimeters	20.4	???	???	???
FBM	20.5	6.697(5)	0.4143(30)	0.9381(5)

TABLE III: Jason Measured $\langle f_c \rangle$ and $\langle f_y \rangle$ (only statistical errors are given) and corresponding $\langle \nu_y \rangle$ calculated via Eq. (2). This data was collected during Run-1. The FBM measurements use the 6 o'clock vertical FBM central fiber (no. 4), where the first 3 µs of data are not used for these measurements.

Detector	V_{quad} [kV]	$\langle f_c \rangle$ [MHz]	$\langle f_y \rangle$ [MHz]	$\langle \nu_y \rangle$
FBM	13.0	6.715(5)	1.8555(50)	0.2763(8)
FBM	15.0	6.715(5)	1.9940(50)	0.2969(8)
trackers	15.0	???	???	???
calorimeters	15.0	???	???	???
FBM	17.6	6.715(5)	2.1680(50)	0.3229(8)
trackers	18.3	???	???	???
calorimeters	18.3	???	???	???
FBM	19.0	6.715(5)	2.2540(50)	0.3357(8)
FBM	20.2	6.715(5)	2.3235(50)	0.3460(8)
trackers	20.4	???	???	???
calorimeters	20.4	???	???	???
FBM	20.5	6.715(5)	2.3370(50)	0.3480(8)

as

$$\nu_x \equiv \mathcal{N}_x = \frac{\mathcal{N}_x/\mathcal{T}}{1/\mathcal{T}} = \frac{f_x}{f_c} = 1 - \frac{f_{\text{cbo}}}{f_c}$$
$$\nu_y \equiv \mathcal{N}_y = \frac{\mathcal{N}_y/\mathcal{T}}{1/\mathcal{T}} = \frac{f_y}{f_c} = \frac{1}{2}\left(1 - \frac{f_{\text{vw}}}{f_c}\right), \tag{2}$$

where $\mathcal{N}_x$ is the number of horizontal betatron oscillations per 1 turn around the storage ring, $\mathcal{T}$ is the time it takes traverse 1 turn around the storage ring, f_x is the horizontal betatron frequency, f_c is the cyclotron frequency, f_{cbo} is the coherent betatron oscillation frequency, $\mathcal{N}_y$ is the number of vertical betatron oscillations per 1 turn around the storage ring, f_y is the vertical betatron frequency, and f_{vw} is the vertical waist frequency.

The V_{quad} settings need to be translated into beam dynamics parameters to help understand the operational behavior of the storage ring. The FBM, trackers, and calorimeters can be used to measure the average cyclotron ($\langle f_c \rangle$), coherent betatron oscillation ($\langle f_{\text{cbo}} \rangle$), vertical betatron ($\langle f_y \rangle$), and vertical waist ($\langle f_{\text{vw}} \rangle$) frequencies. These average frequencies can in turn be used to determine the average horizontal ($\langle \nu_x \rangle$) and vertical ($\langle \nu_y \rangle$) tunes, see Tables II and III.

For a circular storage ring with a perfect dipole magnetic field (B_0), the field index inside of a quadrupole (n_0) is defined as

$$n_0 \equiv \frac{m\gamma r}{pB_0}\frac{\partial E_r}{\partial r}, \tag{3}$$

where m is mass, γ is the Lorentz factor, r is the radial distance from the center of the storage ring, p is momentum, and E_r is the radial component of the quadrupole electric field.

The smoothed quadrupole model describes the EQS as being continuous around the entire storage ring. The effective field index (n) in the smoothed model is defined as

$$n \equiv \left(\frac{4l_q}{C_0}\right) n_0 = \left(\frac{l_q/R_0}{\pi/2}\right) n_0, \tag{4}$$

where $R_0 = 7112$ mm is the storage ring equilibrium orbit radius, $C_0 = 2\pi R_0$ is the storage ring equilibrium orbit circumference, and l_q is the quadrupole long-short pair length.

The smoothed model approximates [**?**] the storage ring tunes as

$$\nu_x \approx \sqrt{1-n}$$
$$\nu_y \approx \sqrt{n}. \tag{5}$$

The discrete quadrupole model describes the EQS as being a set of 4 separate quadrupoles that have a four-fold symmetry around the storage ring. The discrete model approximates [**?**] the storage ring tunes as

$$\cos\left(\frac{\pi}{2}\nu_x\right) \approx c_i \cos\left(\frac{l_q}{R_0}\sqrt{m}\right) - \frac{1}{2}s_i\left(\sqrt{m} + \frac{1}{\sqrt{m}}\right)\sin\left(\frac{l_q}{R_0}\sqrt{m}\right)$$
$$\cos\left(\frac{\pi}{2}\nu_y\right) \approx \cos\left(\frac{l_q}{R_0}\sqrt{n_0}\right) - \frac{1}{2}\frac{l_i}{R_0}\sqrt{n_0}\sin\left(\frac{l_q}{R_0}\sqrt{n_0}\right), \tag{6}$$

where $c_i \equiv \cos(l_i/R_0)$, $s_i \equiv \sin(l_i/R_0)$, $m \equiv 1 - n_0$ and l_i is the interval length between quadrupole long-short pairs. The following numerical relations obtained from [**?**] are assumed for Eq. (6): $l_i/R_0 = 0.895354$, $l_q/R_0 = 0.675442$, and $n_0 = n/0.43$.

Equations (3) and (4) show that $n \propto \partial E_r/\partial r$, and $E_r \propto V_{\text{quad}}$ when assuming that the quadrupole geometry and HV pulse generation are independent of V_{quad}, which then implies that $n \propto V_{\text{quad}}$:

$$n = \sigma V_{\text{quad}}, \tag{7}$$

where σ is the proportionality constant (conversion factor) between n and V_{quad} *[need to pick a different symbol for σ, as it gets confusing when talking about the standard deviation difference]*. Equation (7) is combined with Eqs. (5) and (6), and the resulting functions are fit to the $\langle \nu_x \rangle$ and $\langle \nu_y \rangle$ data in Tables II and III, see Fig 19. The σ_x^s, σ_y^s, σ_x^d, and σ_y^d fit parameters in Fig. 19 correspond to the σ in Eq. (7). In the ideal case, $\sigma_x^s = \sigma_y^s$ and $\sigma_x^d = \sigma_y^d$.

The $\chi^2/\text{ndf} < 1$ for all of the fits in Fig. 19, which indicates that the precision of the fit parameters is limited by the "large" size of the data point errors. There is some mild tension between the horizontal and vertical tune fits within each model, as

$$\begin{aligned} \frac{\left|\sigma_x^s - \sigma_y^s\right|}{\sqrt{\left(\delta_x^s\right)^2 + \left(\delta_y^s\right)^2}} &= 1.990\,\sigma \\ \frac{\left|\sigma_x^d - \sigma_y^d\right|}{\sqrt{\left(\delta_x^d\right)^2 + \left(\delta_y^d\right)^2}} &= 2.147\,\sigma, \end{aligned} \tag{8}$$

where δ_x^s, δ_y^s, δ_x^d, and δ_y^d are the errors for the σ_x^s, σ_y^s, σ_x^d, and σ_y^d values respectively. This tension is likely due to some undetermined systematic effect in the tune data. This tension can be eliminated by rescaling the errors so that the standard deviations difference is $1\,\sigma$, where these multiplicative scale factors are $\epsilon^s = 1.990$ and $\epsilon^d = 2.147$ for the smoothed and discrete models respectively.

The horizontal and vertical fit parameters can be averaged to produce a final estimation of the conversion factor between n and V_{quad}:

$$\begin{aligned} \sigma^s &= \frac{1}{2}\left(\sigma_x^s + \sigma_y^s\right) \pm \frac{1}{2}\sqrt{\left(\epsilon^s \delta_x^s\right)^2 + \left(\epsilon^s \delta_y^s\right)^2} \\ &= (5.886 \pm 0.023) \times 10^{-3}\,\text{kV}^{-1} \\ \sigma^d &= \frac{1}{2}\left(\sigma_x^d + \sigma_y^d\right) \pm \frac{1}{2}\sqrt{\left(\epsilon^d \delta_x^d\right)^2 + \left(\epsilon^d \delta_y^d\right)^2} \\ &= (5.892 \pm 0.025) \times 10^{-3}\,\text{kV}^{-1}, \end{aligned} \tag{9}$$

where σ^s and σ^d are the average conversion factors for the smoothed and discrete models. Equations (8) and (9) show that the smoothed and discrete models produce consistent results, and Table IV provides Run-1 field index and tune values that are based on the smoothed model *[maybe this should also be done for the discrete model]*.

C. Closed Orbit Distortions

Mike

Someone should discuss the closed orbit and beta func-

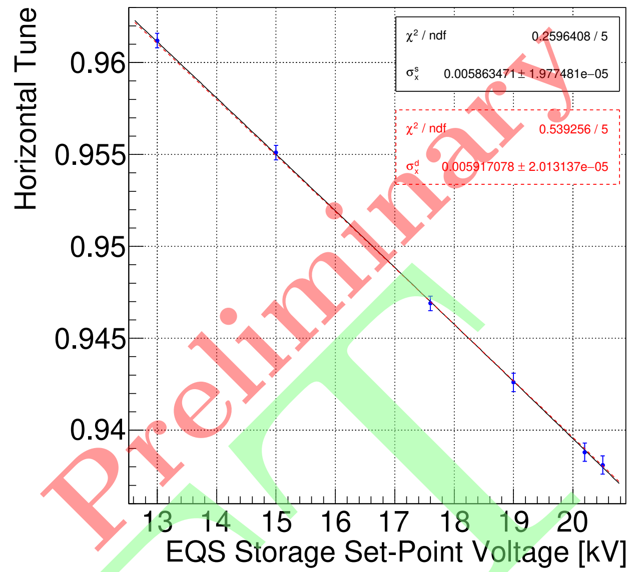

(a) $\langle \nu_x \rangle$ vs. V_{quad}

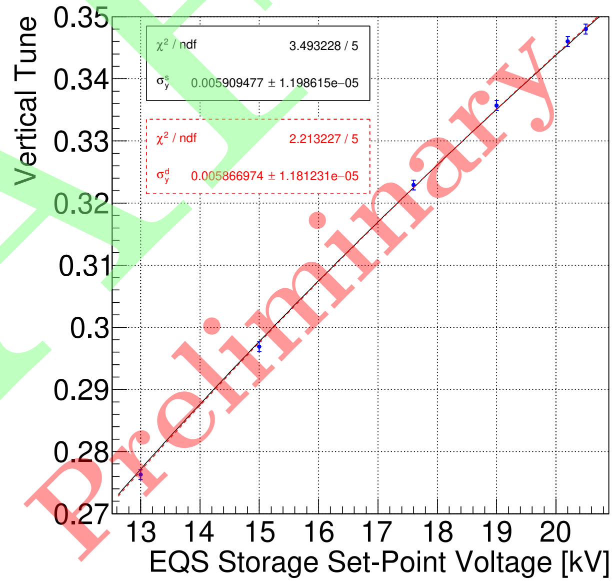

(b) $\langle \nu_y \rangle$ vs. V_{quad}

FIG. 19: Jason Average tune data (blue circular points), see Tables II and III, along with fits using the smoothed quadrupole model (solid black lines) and discrete quadrupole model (red dashed lines), see Eqs. (5), (6), and (7). The σ_x^s, σ_y^s, σ_x^d, and σ_y^d fit parameters are for the smoothed model fit to $\langle \nu_x \rangle$ data, smoothed model fit to $\langle \nu_y \rangle$ data, discrete model fit to $\langle \nu_x \rangle$ data, and discrete model fit to $\langle \nu_y \rangle$ data respectively. Mike and David T. : *Add a set of simulation based tune curves, see DocDB15538 and DocDB16661.*

TABLE IV: Jason Field index and tune values based on the smoothed model for different quadrupole storage voltages used in Run-1 data collection, see Eqs. (5), (7), and (9), along with the numerical relation $n_0 = n/0.43$ obtained from [?].

V_{quad} [kV]	n_0	n	ν_x	ν_y
15.0	0.20533(80)	0.08829(35)	0.95484(18)	0.29714(58)
18.3	0.25050(98)	0.10771(42)	0.94461(22)	0.32820(64)
20.4	0.2792(11)	0.12007(47)	0.93804(25)	0.34652(68)

TABLE V: Mike Quadrupole in situ alignment data *[Mike S. will have to elaborate and the units need checking]*.

Quadrupole	d_{bot} [mm]	d_{top} [mm]	d_{inn} [mm]	d_{out} [mm]
Q1S	2.05	2.42	-0.59	-0.06
Q1L	-0.84	-1.12	-0.53	0.04
Q2S	-0.49	-0.86	-0.70	-1.29
Q2L	0.67	0.09	0.06	-0.13
Q3S	1.16	0.34	-0.40	0.00
Q3L	-1.84	-2.09	0.31	-0.08
Q4S	-1.16	-1.47	1.85	2.24
Q4L	-0.44	0.00	0.20	-0.03

tion distortions due to an imperfect E- and B-field, see Figs. 20 and 21. These results are based on the B-field data shown in Fig. 1 and the E-field effects due to the quadrupole misalignments given in Tables V and VI.

VI. SYSTEMATICS

A. Detector Acceptance & Coherent Beam Motion

Jason

The acceptance of the calorimeters for the decay positron depends on the radial position of the parent muon. The acceptance therefore varies as the centroid of the distribution oscillates and the width is modulated over the course of the fill. The coherent motion of the

TABLE VI: Mike Quadrupole in situ alignment data *[Mike S. will have to elaborate and the units need checking]*.

Quadrupole	dx [mm]	dy [mm]	dax [mm]	day [mm]
Q1S	-0.325	2.235	0.265	0.185
Q1L	-0.245	-0.980	0.285	-0.140
Q2S	-0.995	-0.675	-0.295	-0.185
Q2L	-0.035	0.380	-0.095	-0.290
Q3S	-0.20	0.75	0.20	-0.41
Q3L	0.115	-1.965	-0.195	-0.125
Q4S	2.045	-1.315	0.195	-0.155
Q4L	0.085	-0.220	-0.115	0.220

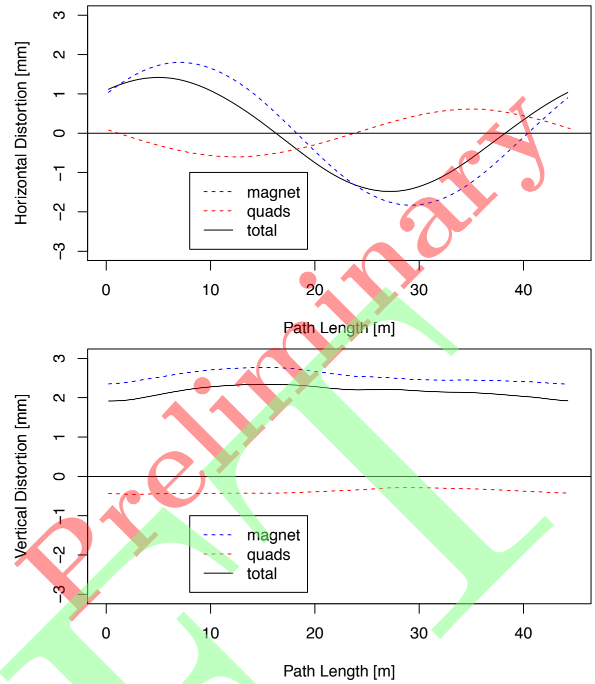

Note: in all of the above, need to check on the initial coordinates for each data set (*i.e.*, where is $\phi = 0$?)

FIG. 20: Mike and David T. Closed orbit distortion *[See DocDB15538 and DocDB16661; combine both figures into one]*.

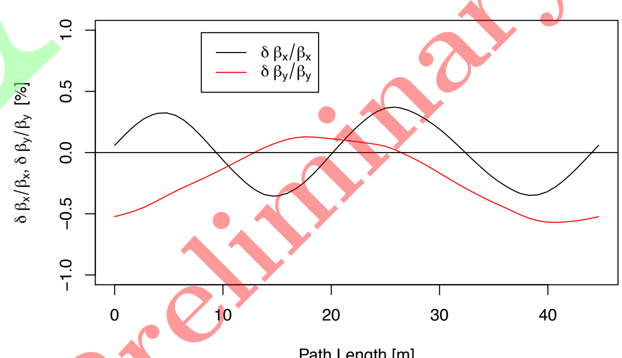

FIG. 21: Mike and David T. Beta function distortion *[See DocDB15538 and DocDB16661]*.

centroid, that results from errors in injection angle and kicker field, and the coherent modulation of the beam width, arising from the phase space mismatch at injection, are characterized by decoherence times. (The coherent motion and modulation early in the fill is evident

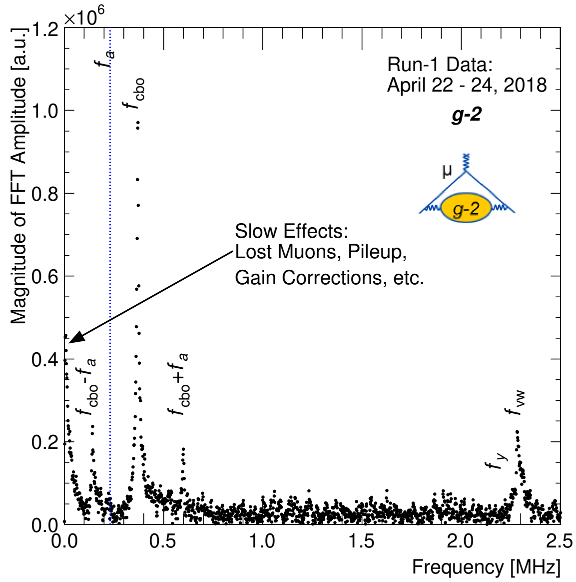

FIG. 22: Jason FFT of 5 parameter fit residuals for a decay positron time spectrum.

for example in Figs. 3 and 5, and the decoherence at later times in Fig. 4). The beam decoheres because of the amplitude and momentum dependence of tunes associated with quadrupole nonlinearity (discussed above) and the chromaticity. But the leading source of decoherence is the large momentum spread and the strong dependence of path length on momentum. The change in circumference due to fractional momentum offset is

$$\frac{\Delta C}{C} \sim \frac{\eta}{R}\frac{\Delta p}{p} \Rightarrow \frac{\Delta p}{p}$$

in the weak focusing limit. The momentum acceptance of the ring is $\Delta p/p \sim \pm 0.125\,\%$. The distribution will lap itself in as few as four hundred turns or 60 µs, effectively mixing the distribution. Indeed a measure of the decoherence time is an indication of the width of the momentum distribution.

Elaborate on the CBO...

Talk about beam frequencies getting into the wiggle plots, see Table VII and Fig. 22.

B. Pitch Correction

David R.

Our measurement of the anomalous precession frequency of the muon depends on the correlation of muon velocity and muon polarization. The projection of polarization onto velocity is given by (Jackson 11.171)

$$\frac{d}{dt}(\hat{\beta}\cdot\mathbf{s}) = -\frac{e}{mc}\mathbf{s}_{\perp}\cdot\left[a_\mu(\hat{\beta}\times\mathbf{B}) + \left(a_\mu - \frac{1}{\gamma^2-1}\right)\beta\mathbf{E}\right] \tag{10}$$

The dependence of ω_a on the amplitude of vertical betatron oscillations appears in the term $\hat{\beta}\times\mathbf{B}$ in Equation 10. If $\mathbf{B} = B\hat{\mathbf{y}}$ and $\hat{\beta} = \sin\psi_{yz}\hat{\mathbf{y}} + \cos\psi_{yz}\hat{\mathbf{z}}$ then $\hat{\beta}\times\mathbf{B} \sim \beta_z B = \beta(\cos\psi_{yz})B$, where ψ_{yz} is the angle of the trajectory in the $y-z$ plane. The contribution to ω_a due to the pitch for a particular trajectory is $\frac{\Delta\omega_a}{\omega_a} = (1-\cos\psi_{yz})$ and for $\psi_{yz} \ll 1$,

$$\frac{\Delta\omega_a}{\omega_a} \sim \frac{1}{2}\psi_{yz}^2,$$

The contribution from the pitch angle averaged over all ϕ for each amplitude a and then over all possible amplitudes a, is

$$\langle\langle\frac{\Delta\omega_a}{\omega_a}\rangle_\phi\rangle_a \sim \frac{1}{2}\langle\langle\psi_{yz}^2\rangle_\phi\rangle_a,$$

In the limit of strictly linear betatron motion, the displacement y is related to amplitude a according to $y = \sqrt{a\beta_y}\cos\phi_y$, where ϕ_y is the betatron phase advance. Then the angle

$$\psi_{yz} = \psi_0\sin\phi = \sqrt{\frac{a}{\beta_y}}\sin\phi_y.$$

The average of ψ_{yz}^2 over all ϕ_y for amplitude a is

$$\langle\psi_{yz}^2(a)\rangle_\phi = \frac{1}{2}\psi_0^2(a) = \frac{\langle y^2(a)\rangle_\phi}{\beta^2}$$

Next, average over all amplitudes a. We suppose that the distribution of amplitudes is given by some function $P(a)$ defined over the physical aperture. Then

$$\langle\langle y^2\rangle_\phi\rangle_a = \frac{1}{2}\beta\frac{\int_{aper} aP(a)da}{\int_{aper} P(a)da}$$

$$\langle\langle\psi^2\rangle_\phi\rangle_a = \frac{1}{2}\langle\psi_0^2\rangle_a = \frac{a}{\beta^2}\langle\langle y^2\rangle_\phi\rangle_a$$

$$C_p \equiv \frac{\Delta\omega_a}{\omega_a} = \frac{1}{4}\langle\psi_0^2\rangle_a = -\frac{n\langle y^2\rangle}{2R_0^2}$$

where $\beta_y = \frac{\sqrt{n}}{R_0}$.

The vertical distribution of decay positrons is measured by the straw tracking chambers. Tracks of positrons are extrapolated back to the parent muon decay point to determine the vertical distribution of the muons as shown for a subset of the data in Fig. 23

C. E-field Correction

David R. The E-field systematic is associated with the third term on the right hand size of Eq. (1) and depends

TABLE VII: Jason Beam frequencies that can affect the decay positron spectra via detector acceptance for $n = 0.137$ *[update with $V_{\text{quad}} = 18.3\,\text{kV}$ values]*.

Frequency	Variable	Expression	Value [MHz]	Corresponding Period [µs]
Anomalous Precession	f_a	$(ea_\mu B_0)/(2\pi m_\mu)$	0.23	4.37
Cyclotron	f_c	$p_0/(2\pi m_\mu \gamma_0 R_0)$	6.71	0.149
Horizontal Betatron	f_x	$\nu_x f_c$	6.23	0.160
Vertical Betatron	f_y	$\nu_y f_c$	2.48	0.402
Coherent Betatron Oscillation	f_{cbo}	$f_c - f_x$	0.48	2.10
Vertical Waist	f_{vw}	$f_c - 2f_y$	1.74	0.57

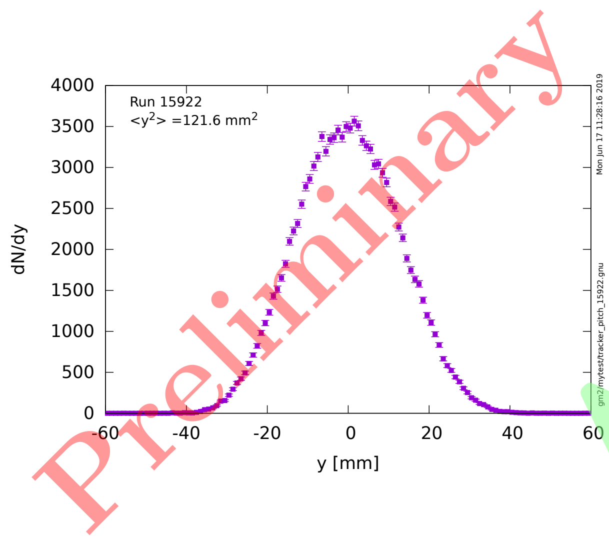

FIG. 23: David R. Vertical distribution measured by straw tracker for a subset of the data. The data is not corrected for acceptance or resolution.

on momentum and radial electric field. The contribution from the electric field is minimized by operating near the magic momentum, namely where $a_\mu = \frac{1}{\gamma^2-1}$ The field of the ring magnet is chosen so that the closed orbit of the magic momentum muon corresponds to the design trajectory. Then the contribution to ω_a is

$$C_e \sim -2\frac{\Delta p}{p_m}\frac{\vec{\beta}\times\vec{E}}{Bc} \tag{11}$$

where p_m is the magic momentum γ and β are evaluated at p_m.

The electric field depends on transverse displacement in the quadrupoles. Insofar as the field is with displacement, the average electric field along the trajectory is proportional to the average radial displacement x_e, namely the closed orbit.

$$\langle E_r\rangle = n\left(\frac{v_s B}{R_0}\right)x_e$$

where n is the focusing index. The average radial displacement is

$$x_e = \eta\frac{\Delta p}{p}.$$

Then the contribution to ω_a due to electric field is

$$C_e \sim -2\beta^2 n(1-n)\frac{x_e^2}{R_0^2}$$

where $\eta =\sim \frac{1-n}{R_0}$. Determination of the E-field correction thus depends on measurement of the equilibrium radial distribution. (The magnitude of the E-field correction is reduced by a few percent due to the nonlinearity of the quadrupole field.)

The radial distribution is determined by a "fast rotation analysis", that exploits the connection between the revolution frequency and the radial displacement. A technique [?] based on Fourier transform yields a frequency spectrum that can be correlated with radius (circumference) and momentum. An alternative method extracts the radial distribution from the measured debunching of the muon beam. The fast rotation data is provided by the calorimeters which measure the time dependence of the intensity of the distribution. An example of radial (closed orbit) distribution extracted by both the Fourier method and the debunching analysis are shown in Fig. 24. The dependence of the E-field contribution to ω_a, on the radial offset of the closed orbit, superimposed on the the measured distribution is shown in Fig. 25.

D. Early-to-late Effects

Bill

The clock starts at t_0. The muons enter the ring with some distribution of times with respect to t_0. We measure the polarization as a function of time. If we measure polarization at time t, polarization of muons that entered the ring at the head of the muon pulse (that enter the ring at times $t_{ini} < t_0$ will have precessed a bit more than those at the tail of the bunch. The difference in their precession will correspond to a phase shift. What is fitted is the oscillation of the distribution. If different parts of the distribution have different phase it will not effect the fitted frequency. But suppose the particles

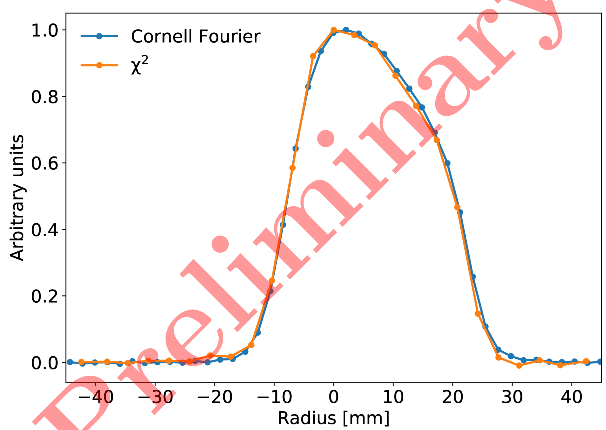

FIG. 24: David R. Fourier analysis of the fast rotation signal and parametererized fit give the muon equilibrium radial (closed orbit) distributionrevolution.

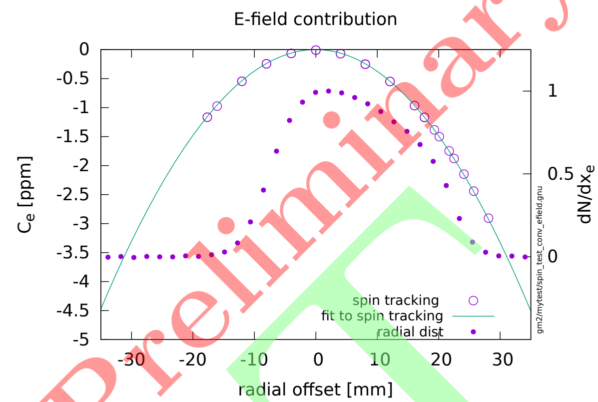

FIG. 25: David R. The contribution to ω_a (C_e) due to the electric field is computed by spin tracking as a function of muon momentum and plotted in terms of the closed orbit. The measured radial distribution is superimposed. The average correction is the convolution of the two.

at the head and tail of the pulse have different energies. High momentum muons survive longer than low momentum muons. Now the average precession phase of the distribution will vary with time, introducing a systematic error in the measurement of the frequency. There are a couple of mechanisms for introducing an early to late momentum dependence. Energy acceptance depends on kicker field. And the kicker field is not uniform over the length of the bunch. That gives us a correlation with energy along the bunch. Also, there may be a momentum spin correlation introduced upstream as part of the pi-mu production mechanism *(see docdb 3693)*. Δt_{ini}

Say something about differential decay???

E. Spin Resonances

Volodya

Someone should say something about the spin resonance lines, see Fig. 26.

F. Lost Muons

Sudeshna

During the first couple of hundred turns after injection, muons outside the aperture defined by the collimators are scraped out, and ideally particles that survive scraping will be lost only to decay. There may however be some particles with long time scale unstable motion, perhaps associated with a resonance (Fig. 27), that eventually exit. Particles may also be lost to scattering from residual gas. If there is any correlation of these lost muons with the parameters of the muon phase space, the distribution will change with time and confuse our corrections. If the lost muons populate a portion of the phase space that is correlated with momentum or position, the phase space of muons contributing to the measurement of polarization will be distorted. the difference frequency will change as the lost particles are lost.

The phase space volume of the injected muon distribution overwhelms the ring acceptance. As a result, the distribution that is stored fills the aperture. Muons at the edge of the momentum or transverse aperture may be lost over the course of a fill. If those losses correlate with any particular region of the muon phase space or polarization, there will be a systematic distortion on the measurement of momentum and/or phase space distribution and/or ω_a phase [**?**]. If for example, high momentum muons are lost early in the fill by hitting an aperture, there will be a systematic shift of the ω_a phase over the course of the fill as the lower momentum muons in the distribution decay away. Or if particles with large vertical oscillation are lost, the pitch correction can be skewed.

In order to insure that all circulating muons are well within the aperture defined by the collimators, muons at the edge of the aperture are scraped at the start of the fill. The scraping is accomplished by adjusting the voltages on the quadrupole plates asymmetrically, thereby introducing an electrostatic dipole moment, that displaces the

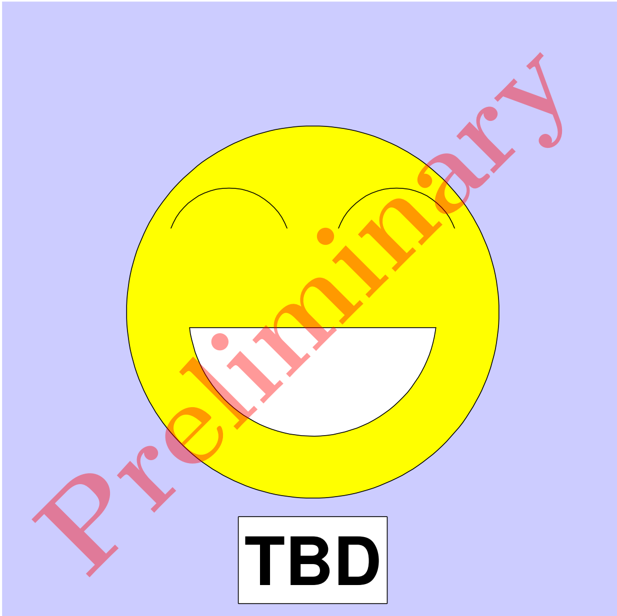

FIG. 26: Jason Betatron tune plane with spin resonance lines.

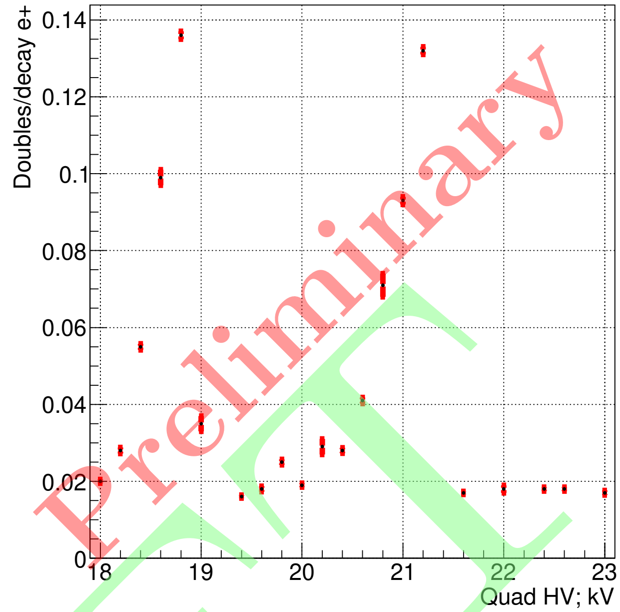

FIG. 27: Sudeshna Fraction of lost muons as a function of EQS storage set-point voltage for calorimeter 1. An increased lost muon rate is observed from the betatron resonances centered near 18.8 and 21.2 kV. These resonances are due to the $3\nu_y = 1$ and $\nu_x + 2\nu_y = 2$ lines in the tune plane.

closed orbit by about 2 mm both vertically and radially from the center of the aperture. The asymmetric voltages are sustained for 7 µs (many betatron periods) and then the closed orbit is restored adiabatically. The vertical displacement of the distribution is measured by the traceback detectors (see Fig. 28) at a point in the ring 180° beyond the injection point and over the course of the scraping cycle. The remaining distribution on the restored closed orbit will nominally have at least 1 mm clearance with respect to the collimators. Muons that are lost are identified as a double (or triple) coincidence in adjacent calorimeters so that the effectiveness of the scraping procedure can be confirmed.

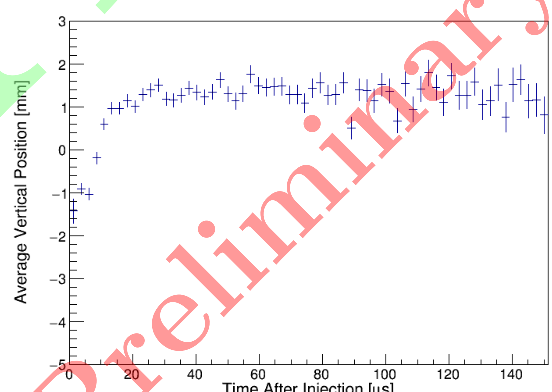

FIG. 28: David R. Vertical displacement of the centroid at the 180° tracker during the scraping cycle.

VII. CONCLUSION

Jason

A quantitative understanding of the evolution of the muon distribution over the course of the fill is essential to limiting the systematic uncertainty in the measurement of the anomalous magnetic moment to the 70 ppb (systematic) target. The experiment is equipped with detectors that can measure phase space and momentum distribution in some detail, as we have demonstrated with a few examples. Beam dynamics simulations informed by the measurements complete the description. The preliminary data presented above was collected during the commissioning phase of the experiment. Nevertheless it is clear that the fiber harp and tracker systems are an extraordinary window on the behavior of the circulating distribution.

ACKNOWLEDGMENTS

Jason

We thank E989 Collaborators, the Fermi National Accelerator Laboratory, a U.S. Department of Energy, Office of Science, HEP User Facility for the resources provided. Fermilab is managed by the Fermi Research Alliance, LLC(FRA), acting under Contract No. DE-AC02-07CH11359. The authors are supported by the US NSF, and the UK STFC. I also wish to thank all of our colleagues who made this experiment and these measurements possible and with whom I have benefited from countless discussions.

[] J. Crnkovic *et al.*, Commissioning the Muon g-2 Experiment Electrostatic Quadrupole System, in *Proc. 9th International Particle Accelerator Conference (IPAC'18), Vancouver, BC, Canada, April 29-May 4, 2018*, International Particle Accelerator Conference No. 9 (JACoW Publishing, Geneva, Switzerland, 2018) pp. 1848–1851.

[] J. Grange *et al.* (Muon g-2), Muon (g-2) Technical Design Report, (2015), arXiv:1501.06858 [physics.ins-det].

[] D. Sagan, Bmad: A relativistic charged particle simulation library, *Computational accelerator physics. Proceedings, 8th International Conference, ICAP 2004, St. Petersburg, Russia, June 29-July 2, 2004*, Nucl. Instrum. Meth. **A558**, 356 (2006).

[] Y. K. Semertzidis *et al.*, The Brookhaven muon (g-2) storage ring high voltage quadrupoles, Nucl. Instrum. Meth. **A503**, 458 (2003).

[] A. Schreckenberger *et al.*, New Fast Kicker Results from the Muon g-2 E-989 Experiment at Fermilab, in *Proc. 9th International Particle Accelerator Conference (IPAC'18), Vancouver, BC, Canada, April 29-May 4, 2018*, International Particle Accelerator Conference No. 9 (JACoW Publishing, Geneva, Switzerland, 2018) pp. 4879–4881.

[] Y. Orlov *et al.*, Muon revolution frequency distribution from a partial-time Fourier transform of the g-2 signal in the muon g-2 experiment, Nucl. Instrum. Meth. **A482**, 767 (2002).